Ferroelectric-Domain-Patterning-Controlled Schottky Junction State in Monolayer MoS_{2}

Zhiyong Xiao, Jingfeng Song, David K. Ferry, Stephen Ducharme, and Xia Hong

Phys. Rev. Lett. **118**, 236801 — Published 8 June 2017

DOI: 10.1103/PhysRevLett.118.236801

Ferroelectric Domain Patterning Controlled Schottky Junction State in Monolayer MoS_2

Zhiyong Xiao[1,2], Jingfeng Song[1,2], David K. Ferry[3], Stephen Ducharme[1,2], Xia Hong[1,2*]

[1] Department of Physics and Astronomy, University of Nebraska-Lincoln, NE 68588-0299, USA

[2] Nebraska Center for Materials and Nanoscience, University of Nebraska-Lincoln, NE 68588-0299, USA

[3] School of Electrical, Computer, and Energy Engineering, Arizona State University, Tempe, Arizona 85287-5706, USA

ABSTRACT:

We exploit for the first time scanning probe controlled domain patterning in a ferroelectric top-layer to induce nonvolatile modulation of the conduction characteristic of monolayer MoS_2 between a transistor and a junction state. In the presence of a domain wall, MoS_2 exhibits rectified *I-V* that is well described by the thermionic emission model. The induced Schottky barrier height Φ_B^{eff} varies from 0.38 eV to 0.57 eV and is tunabe by a SiO_2 global back-gate, while the tuning range of Φ_B^{eff} depends sensitively on the conduction band tail trapping states. Our work points to a new route to achieve programmable functionalities in van der Waals materials and sheds light on the critical performance limiting factors in these hybrid systems.

Monolayer (ML) transition metal dichalcogenide (TMDC) MX_2 (M = Mo, W; X = S, Se, Te) possesses atomic thickness, highly tunable electronic states, and direct band gaps of 1-2 eV [1], making them a versatile playground for imposing nanoscale band structure design [2] and building novel homo- and hetero-junctions for nanoelectronic [3-6] and optoelectronic applications [7-9]. TMDC-based Schottky and *p*-*n* junctions have previously been achieved by exploiting multiple local gates [9, 10], electric-double-layer gating controlled bipolar carrier injection [11], contact work function engineering [12, 13], or exploring van der Waals heterostructures [14-16], where the device functionalities cannot be altered after fabrication. On the other hand, the ability to create well-defined but reconfigurable potential barriers at the nanoscale can be utilized to disentangle the intricate interplay of various impurity sources and the dielectric environment in determining the electronic and optical response of TMDC in the junction state, as well as achieving multifunctional operations on a single two-dimensional (2D) platform.

A promising approach to locally define the potential profile and produce a programmable junction state in TMDCs is to capitalize on the nonvolatile, switchable polarization field of a ferroelectric gate. The ferroelectric field effect has previously been intensively investigated in layered van der Waals materials such as graphene and TMDCs for building novel logic and memory devices [17-20], tunnel junctions [21], sensors [22-24], and plasmonic and optoelectronic applications [25-28]. However, the unique opportunity offered by nanoscale polarization control, which can lead to local carrier density modulation in the 2D channel, has yet to be explored. In this study, by domain patterning in an ultrathin ferroelectric polymer top-layer via scanning probe microscopy, we have achieved for the first time programmable transistor and Schottky junction states in a single channel of ML MoS_2. In the mono-domain

states, we observed ohmic source-drain current-voltage (I_{DS}-V_{DS}) relation for both the polarization up (P_{up}) and down (P_{down}) states. Modeling the transfer characteristics shows that the free electron band mobility of the sample is limited by charged impurity (CI) scattering, which is not affected by polarization switching. In the presence of a ferroelectric domain wall (DW) perpendicular to the current direction (denoted as the half P_{up}-half P_{down} state), the channel exhibits rectified *I-V* that can be well described by the thermionic emission model, with the induced Schottky barrier height Φ_B^{eff} further tunable by a SiO_2 global back-gate.

We fabricated ML MoS_2 field effect transistor (FET) devices sandwiched between a 300 nm SiO_2 global back-gate and a ferroelectric top layer (17.8±0.7 nm) of poly(vinylidene fluoride-trifluoroethylene) [P(VDF-TrFE)] (Fig. 1(a)), where the copolymer films were deposited using the Langmuir-Blodgett (LB) technique [29-31]. Unlike the thick P(VDF-TrFE) films prepared by spin-coating [17, 18, 22, 26], the ultrathin LB films possess smooth surfaces (~1 nm surface roughness) and low coercive voltage (< 10 V), making it possible to write and image ferroelectric domains with nanoscale precision via the conductive probe atomic force microscopy (AFM) and piezo-response force microscopy (PFM) [37, 38]. The reported electrical results were based on 6 MoS_2 samples, denoted as D1-D6.

Figure 1(b) shows the room-temperature transfer characteristic of sample D2 gated through SiO_2 (Fig. 1(c)). With increasing back-gate voltage V_{bg}, I_{DS} exhibits an exponential growth at low V_{bg} followed by a quasi-linear gate-dependence beyond a transition voltage (denoted as V_t), signaling the shift of the Fermi level E_F from well residing in the bandgap to close to the conduction band edge. We extracted the field effect mobility of the sample from the linear region of $I_{DS}(V_{bg})$ as $\mu_{FE} = \frac{1}{e\gamma}\frac{L}{W}\left(dG/dV_{bg}\right)$, where γ= 7.2x10^{10} cm^{-2}V^{-1} is the gating efficiency of 300 nm SiO_2, $G = I_{DS}/V_{DS}$ is the channel conductance, and L (W) is the channel length (width). As

there is no metal-electrode on P(VDF-TrFE), the presence of the ferroelectric top-layer does not change γ, as demonstrated in previous studies of SiO_2-gate graphene with ice [39] and HfO_2 [40] top-layers. In the as-deposited state, the sample exhibits μ_{FE} of 6.7 $cm^2V^{-1}s^{-1}$ and V_t of -20 V.

To control the out-of-plane polarization of the copolymer, we apply a constant bias voltage higher than the coercive voltage to a conductive AFM tip while it is scanning on the sample surface in the contact mode (Fig. 1(a)). We first switched the copolymer to the uniform P_{down} state by writing the entire channel area with a tip bias V_{tip} of +10 V while keeping MoS_2 grounded. The PFM phase image (Fig. 1(d)) shows that P(VDF-TrFE) on top of the device area has been uniformly polarized, while the portion on top of the SiO_2 substrate remains unpoled. In the P_{down} state, electrons are accumulated in MoS_2, which shifts E_F towards the conduction band edge, yielding a nonvolatile offset in the doping level. The resulting transfer curve shifts to the negative V_{bg} direction, with corresponding μ_{FE} of 4.7 $cm^2V^{-1}s^{-1}$ and V_t of -38 V.

We then polarized the ferroelectric top-layer to the uniform P_{up} state (Fig. 1(e)) by scanning the entire sample area with V_{tip} = -10 V, depleting electrons from MoS_2. The resulting I_{DS}-V_{bg} curve shifts to the positive V_{bg} direction with V_t = -12 V. The slightly lower μ_{FE} of 3.3 $cm^2V^{-1}s^{-1}$ is due to the reduced screening of CIs in the depletion state. The scanning probe controlled polarization switching is nonvolatile and fully reversible. The third AFM writing with V_{tip} = +10 V poled the copolymer back to the uniform P_{down} state, and the resulting transfer curve of MoS_2 overlaps with that of the first poling. The switching ratio between the high (P_{down}) and low (P_{up}) conductance states reaches ~450 at V_{bg} = -25 V.

In previous studies of ferroelectric-gated TMDC, despite the tremendous progress in developing various nanoelectronic/optoelectronic devices [17-22, 25, 26], in-depth understanding is yet to be gained on how the ferroelectric layer affects the mobility of the TMDC

channel, e.g., regarding the presence of a charged interface, the remote interfacial polar (RIP) phonon, and the polarization reversal. To assess these ferroelectric-specific factors, we have quantitatively modeled the transfer characteristics of MoS_2 in both polarization states. The temperature-dependence of I_{DS} shows that E_F for both polarization states lies in the band gap (E_g) for the entire gating-range [31]. It is thus important to consider in the modeling the conduction band tail trapping states within the gap region as well as the localized states above the conduction band edge, which have been attributed to the charged impurities such as S vacancies in MoS_2 and CIs from the dielectric environment [6]. To account for these midgap states, we incorporated the density of states (DOS) distribution in MoS_2 proposed in Ref. [6]:

$$D_n(E) = \begin{cases} \alpha D_0 \exp\left[-\dfrac{E - E_D}{\varphi}\right] & E_D - \dfrac{E_g}{2} < E < E_D \\ D_0 - (1-\alpha) D_0 \exp\left[-\dfrac{E - E_D}{\varphi'}\right] & E > E_D \end{cases}. \quad (1)$$

Here D_0~3.9x10^{14} eV^{-1}cm^{-2} is the 2D DOS for crystalline MoS_2, E_D is the conduction band edge, φ is the characterization depth of the band tail, and α and φ' are fitting parameters. Using Eq. (1), we first modeled the V_{bg}-dependence of the total carrier density n_{total} and the free electron density n_{free} for sample D3 in both polarization states at $V_{bg} > V_t$ (Fig. 2(a)) [31]. Here n_{total} includes both trapped/localized electrons and n_{free}, with $\Delta n_{total} = \gamma \Delta V_{bg}$. For n_{free}, we only consider the extended states above the mobility edge energy E_M with respect to the conduction band edge:

$$n_{free}(300K) = \int_{E_M}^{\infty} D_n(E) f(E, 300K)\, dE, \quad (2)$$

where $D_n(E)$ is given by Eq. (1) and $f(E)$ is the Fermi-Dirac distribution. We adopted the parameters of φ =110 meV and E_M = 10 meV reported in Ref. [6], as our samples possess similar mobility values.

Figure 2(b) shows the free electron band mobility $\mu_{band} = \sigma / n_{free} e$ as a function of n_{free}, which reveals two important points. First, even though the field effect mobility in this region is a constant (i.e., $I_{DS}(V_{bg})$ is linear), the band mobility associated with the free electrons actually increases linearly with increasing n_{free} for both polarization states, reaching ~10 $cm^2V^{-1}s^{-1}$ at n = $1x10^{11}$ cm^{-2}. This suggests CI scattering rather than phonon scattering as the dominant mobility limiting mechanism [41], since the increased density can enhance the screening of the CIs, resulting in higher mobility. Using Boltzmann transport theory with relaxation time approximation, we find this mobility level corresponds to a CI density N_i ~$3x10^{12}/cm^2$ [31], comparable with the value obtained in MoS_2 sandwiched between SiO_2 and HfO_2. It further confirms that the parameters for the band tail states and mobility edge in Ref. [6] can give a reasonable description of the charge trapping/localization in our samples. Our device mobility extracted from the gap region is also consistent with the high density mobility values reported in literature for MoS_2 on SiO_2 [6, 42-44], as discussed in the Supplementary Materials [31]. At this low density range, scattering from intrinsic acoustic and non-polar optical phonons in MoS_2 is negligibly small. Despite the high dielectric constant of P(VDF-TrFE) ($\varepsilon_{PVDF} = 10$), its RIP phonon also does not play a critical role in limiting the mobility of MoS_2, in stark contrast with other high-k dielectrics such as HfO_2 and Al_2O_3 [41]. While P(VDF-TrFE) can provide effective dielectric screening to the RIP modes of SiO_2, its most active optical phonon modes have $\hbar\omega$ = 63 and 109 meV [45], and the corresponding RIP modes would not contribute as strongly as that of SiO_2 at room temperature [46]. Second, at the same n_{free}, the sample possesses similar mobility values for both polarization states, indicating that switching the polarization direction does not introduce additional scatterers. This is understandable since the switchable polarization originates from the crystalline fraction of P(VDF-TrFE), which imposes a periodic polarization

field that does not scatter electrons.

We next explored the possibility of creating a potential barrier in the MoS_2 channel by writing a ferroelectric DW perpendicular to the current direction. In the mono-domain states, despite the large current modulation, we observe linear, ohmic-like I_{DS}-V_{DS} characteristics for both polarization states within V_{DS} = ±100 mV (Fig. 3(a)) over the entire V_{bg} range for all samples investigated. In sharp contrast, when P(VDF-TrFE) was patterned into two domains with opposite out-of-plane polarization directions (Fig. 3(b) inset), at the same V_{bg} of -10 V, sample D4 exhibits rectified nonlinear conduction with much weaker variation in I_{DS} at reverse-bias (Fig. 3(b)). Such nonlinearity can be further tuned by V_{bg}. Figure 3(c) shows the color contour of I_{DS} normalized to the value at V_{DS} = +100 mV versus V_{DS} and V_{bg} for this sample, which exhibits a clear evolution between two distinct behaviors with increasing V_{bg}. At low V_{bg} (region I: V_{bg} < -12.5 V), we observe a linear ohmic-like I_{DS}-V_{DS} relation. At the intermediate V_{bg} range (region II: -12.5 V ≤ V_{bg} ≤ 0 V), I_{DS} exhibits the rectified, diode-like I_{DS}-V_{DS} behavior. Further increasing V_{bg} to region III recovers the linear conduction.

To understand the origin of the evolved I_{DS}-V_{DS} characteristic, we superimposed on Fig. 3(c) the transfer curves of this sample in the mono-domain states. The corresponding transition voltages are V_t = -13 V for P_{down} and V_t = 0 V for P_{up} state, which are in excellent agreement with the boundary V_{bg} voltages that separate regions I, II and III, suggesting that it is the band alignment between the P_{up} and P_{down} sides of the channel that determines the conduction characteristic. When the sample is gated into region I, E_F for both sides is deep in the gap region, leading to high channel resistance. We expect an intrinsic to *n*-doped type interface, and the channel conduction can be modeled as two resistors R_{down} and R_{up}, corresponding to the P_{down} and P_{up} domains, respectively, in series connection. In region II, E_F for the P_{down} side of the

channel is approaching the conduction band edge, so MoS_2 is doped with a high density of free electrons in the extended states at room temperature, while the P_{up} side of the channel remains in the semiconducting state. We thus expect a Schottky junction forming in the vicinity of the DW, with the effective barrier height Φ_B^{eff} corresponding to the difference in E_F between the P_{up} and P_{down} sides (Fig. 4(a) inset). Similarly, well within region III, both sides of the channel are doped with high densities of electrons, yielding low channel resistance with linear conduction.

In region II, we need to consider the additional junction contribution in series connection with R_{up} and R_{down} to model the total channel conduction. We quantitatively modeled the rectified *I-V* in region II using the thermionic emission model [13, 47]:

$$I_{DS} = A_{2D}^{*} T^{3/2} W \exp\left(-\frac{e\Phi_B^{eff}}{k_B T}\right)\exp\left(\frac{eV_{DS}}{nk_B T}\right)\left[1-\exp\left(-\frac{eV_{DS}}{k_B T}\right)\right] \quad (3)$$

with $A_{2D}^{*} = \left[\left(eM_c k_B^{3/2}\right)/\left(\pi\hbar^2\right)\right]\left(m_t^{*}/2\pi\right)^{1/2}$,

where W is the width of the conduction channel, n is the ideality factor, which is normally between 1 and 2, and $m_t^{*} = 0.45m_0$ is the transverse electron effective mass for ML MoS_2 [3]. Here A_{2D}^{*} is the 2D effective Richardson constant, with the number of equivalent conduction band minima $M_c = 2$. Figures 4(a)-(b) show the I_{DS}-V_{DS} curves taken on sample D5 in region II (between V_{bg} = -12 V and 0 V for this sample). At V_{bg} = -10 V, the channel conduction can be well described by Eq. (3) with Φ_B^{eff} = 0.51 eV, which can be further tuned by V_{bg}. The domain patterning induced junction states have been observed in all four samples investigated (D3-D6), with the ideality factor n ranging from 1.4 to 1.8, consistent with previously reported results [9, 12].

The fact that Eq. (3) can give an accurate description of the conduction characteristic indicates that the resistive contribution of R_{down} and R_{up} is also absent at V_{bg} = -10 V. As MoS_2

exhibits more than one order of magnitude change in conductance between the two polarization states in region II (Figs. 1(b) and 3), it is reasonable to neglect R_{down}. The absence of R_{up}, on the other hand, suggests that the extension of the junction transition region is comparable with or larger than the P_{up} side channel length at low carrier density. At sufficiently high V_{bg} ($V_{bg} \geq$ -6 V), when the junction width decreases with increasing carrier density and becomes shorter than the associated channel length, Eq. (3) can no longer provide a satisfactory fit to I_{DS}-V_{DS}. Rather, the conduction has to be modeled as a Schottky junction in series connection with a resistor [31]:

$$V_{DS}^{'} = V_{DS}(I_{DS}) + I_{DS}R_{up}, \quad (4)$$

where $V_{DS}(I_{DS})$ is defined by Eq. (3). Figure 4(b) shows the fit for the I_{DS}-V_{DS} curve at V_{bg} = -4 V to this model, where the first term yields a barrier height of Φ_B^{eff} = 0.43 eV. Comparing the extracted R_{up} with the channel resistance in the uniform P_{up} state yields a channel length of 23 nm, much shorter than the associated P_{up} domain length (350 nm), confirming that on the P_{up} side the junction transition region extends well beyond the vicinity of the DW.

As a control experiment, we erased the domain structure by thermally heating the sample in vacuum to 80 °C, close to its Curie temperature, for 2 hours. The copolymer film then recovers its as-deposited state with polarization randomly orientated, which can be attributed to its low DW energy [38]. After thermal depolarization, the I_{DS}-V_{DS} curve at V_{bg} = -10 V agrees well with that in the as-deposited state (Fig. 4(c)), indicating that the observed junction state is resulting from the ferroelectric domain patterning and the sample quality is preserved during the polarization switching.

As the Schottky barrier height Φ_B^{eff} is defined by the band alignment between the P_{down} and P_{up} states (Fig. 4(a) inset), it can be further tuned by V_{bg}. Figure 4(d) shows Φ_B^{eff} as a function of

the normalized back-gate voltage $(V_{bg}-V_{mid})/V_W$ for samples D3-D6, where V_{mid} and V_w are the middle point and width of region II, respectively. All samples exhibit consistent V_{bg}-dependence of Φ_B^{eff}, which decreases with increasing V_{bg} by 90-150 meV. This reduction in Φ_B^{eff} is a consequence of the high density of states close to the MoS_2 conduction band edge, which results in a moderate change of E_F on the P_{down} side where the sample is doped close to the conduction band.

At the low V_{bg} end of region III, close to the boundary with region II, the channel conduction still exhibits slight nonlinearity but can no longer be properly modeled by Eq. (4) [31], even though the P_{up} state E_F is still about 0.4-0.5 eV below the extended states (Fig. 4(d)). This can be well explained by the band tail states described by Eq. (1), which would limit the gate-tunable range of Φ_B^{eff}, or the width of region II (V_w). As shown in Ref. [6], these impurity states can extend to up to 0.4-0.5 eV below the conduction band of MoS_2, and can contribute to hopping-type conduction, which naturally explains the lack of a well-defined energy barrier at this gating range. Overall, a range of Φ_B^{eff} from 0.38 eV to 0.57 eV has been realized in our samples.

In conclusion, we have demonstrated that nanoscale domain patterning can be utilized to reversibly tune the functionality of a 2D channel, while polarization switching does not affect the channel mobility. This approach can be applied to a wide range of van der Waals materials to design various homojunctions and nanostructures, such as nanoribbons, nanodots and superlattices. Compared to the lithographical methods, the nonvolatile field effect allows one to impose different functional designs on the same 2D platform without introducing disordered interface/edge states. It also opens up the opportunity to integrate logic, memory, and photovoltaic functionalities in a single material platform for nanoelectronic and optoelectronic applications.

Acknowledgments

We would like to thank Zhixian Zhou for insightful discussions, Dawei Li and Peter Kosch for experimental assistance, and Yongfeng Lu for the access to the Raman system. This work was supported by the National Science Foundation (NSF) through Nebraska Materials Research Science and Engineering Center (MRSEC) (Grant No. DMR-1420645) (ferroelectric polymer deposition and device fabrication), NSF CAREER Grant No. DMR-1148783 (electrical and optical characterizations) and NSF Grant No. OIA-1538893 (scanning probe studies), and the U.S. Department of Energy (DOE), Office of Science, Basic Energy Sciences (BES), under Award No. DE-SC0016153 (low temperature studies). The research was performed in part in the Nebraska Nanoscale Facility: National Nanotechnology Coordinated Infrastructure and the Nebraska Center for Materials and Nanoscience, which are supported by NSF under Award ECCS: 1542182, and the Nebraska Research Initiative.

References

[1] Q. H. Wang, K. Kalantar-Zadeh, A. Kis, J. N. Coleman, and M. S. Strano, Electronics and optoelectronics of two-dimensional transition metal dichalcogenides, Nature Nanotechnology **7**, 699 (2012).

[2] A. K. Geim, and I. V. Grigorieva, Van der Waals heterostructures, Nature **499**, 419 (2013).

[3] Y. Yoon, K. Ganapathi, and S. Salahuddin, How Good Can Monolayer MoS_2 Transistors Be?, Nano Letters **11**, 3768 (2011).

[4] B. Radisavljevic, A. Radenovic, J. Brivio, V. Giacometti, and A. Kis, Single-layer MoS_2 transistors, Nature Nanotechnology **6**, 147 (2011).

[5] D. Jariwala, V. K. Sangwan, L. J. Lauhon, T. J. Marks, and M. C. Hersam, Emerging Device Applications for Semiconducting Two-Dimensional Transition Metal Dichalcogenides, Acs Nano **8**, 1102 (2014).

[6] W. J. Zhu, T. Low, Y. H. Lee, H. Wang, D. B. Farmer, J. Kong, F. N. Xia, and P. Avouris, Electronic transport and device prospects of monolayer molybdenum disulphide grown by chemical vapour deposition, Nature Communications **5**, 3087 (2014).

[7] Z. Yin, H. Li, H. Li, L. Jiang, Y. Shi, Y. Sun, G. Lu, Q. Zhang, X. Chen, and H. Zhang, Single-Layer MoS_2 Phototransistors, ACS Nano **6**, 74 (2012).

[8] F. H. L. Koppens, T. Mueller, P. Avouris, A. C. Ferrari, M. S. Vitiello, and M. Polini, Photodetectors based on graphene, other two-dimensional materials and hybrid systems, Nature Nanotechnology **9**, 780 (2014).
[9] B. W. H. Baugher, H. O. H. Churchill, Y. F. Yang, and P. Jarillo-Herrero, Optoelectronic devices based on electrically tunable p-n diodes in a monolayer dichalcogenide, Nature Nanotechnology **9**, 262 (2014).
[10] D. J. Groenendijk, M. Buscema, G. A. Steele, S. M. de Vasconcellos, R. Bratschitsch, H. S. J. van der Zant, and A. Castellanos-Gomez, Photovoltaic and Photothermoelectric Effect in a Double-Gated WSe_2 Device, Nano Letters **14**, 5846 (2014).
[11] S. Jo, N. Ubrig, H. Berger, A. B. Kuzmenko, and A. F. Morpurgo, Mono- and Bilayer WS_2 Light-Emitting Transistors, Nano Letters **14**, 2019 (2014).
[12] S. Chuang, C. Battaglia, A. Azcatl, S. McDonnell, J. S. Kang, X. Yin, M. Tosun, R. Kapadia, H. Fang, R. M. Wallace, and A. Javey, MoS_2 P-type Transistors and Diodes Enabled by High Work Function MoO_x Contacts, Nano Letters **14**, 1337 (2014).
[13] J. Wang, D. Rhodes, S. Feng, M. A. T. Nguyen, K. Watanabe, T. Taniguchi, T. E. Mallouk, M. Terrones, L. Balicas, and J. Zhu, Gate-modulated conductance of few-layer WSe_2 field-effect transistors in the subgap regime: Schottky barrier transistor and subgap impurity states, Applied Physics Letters **106**, 152104 (2015).
[14] C. H. Lee, G. H. Lee, A. M. van der Zande, W. C. Chen, Y. L. Li, M. Y. Han, X. Cui, G. Arefe, C. Nuckolls, T. F. Heinz, J. Guo, J. Hone, and P. Kim, Atomically thin p-n junctions with van der Waals heterointerfaces, Nature Nanotechnology **9**, 676 (2014).
[15] Y. X. Deng, Z. Luo, N. J. Conrad, H. Liu, Y. J. Gong, S. Najmaei, P. M. Ajayan, J. Lou, X. F. Xu, and P. D. Ye, Black Phosphorus-Monolayer MoS_2 van der Waals Heterojunction p-n Diode, ACS Nano **8**, 8292 (2014).
[16] F. Withers, O. Del Pozo-Zamudio, A. Mishchenko, A. P. Rooney, A. Gholinia, K. Watanabe, T. Taniguchi, S. J. Haigh, A. K. Geim, A. I. Tartakovskii, and K. S. Novoselov, Light-emitting diodes by band-structure engineering in van der Waals heterostructures, Nature Materials **14**, 301 (2015).
[17] X. Hong, Emerging ferroelectric transistors with nanoscale channel materials: the possibilities, the limitations, Journal of Physics: Condensed Matter **28**, 103003 (2016).
[18] H. S. Lee, S. W. Min, M. K. Park, Y. T. Lee, P. J. Jeon, J. H. Kim, S. Ryu, and S. Im, MoS_2 Nanosheets for Top-Gate Nonvolatile Memory Transistor Channel, Small **8**, 3111 (2012).
[19] A. Nguyen, P. Sharma, T. Scott, E. Preciado, V. Klee, D. Sun, I. H. D. Lu, D. Barroso, S. Kim, V. Y. Shur, A. R. Akhmatkhanov, A. Gruverman, L. Bartels, and P. A. Dowben, Toward Ferroelectric Control of Monolayer MoS_2, Nano letters **15**, 3364 (2015).
[20] C. Zhou, X. Wang, S. Raju, Z. Lin, D. Villaroman, B. Huang, H. L.-W. Chan, M. Chan, and Y. Chai, Low voltage and high ON/OFF ratio field-effect transistors based on CVD MoS_2 and ultra high-k gate dielectric PZT, Nanoscale **7**, 8695 (2015).
[21] H. Lu, A. Lipatov, S. Ryu, D. J. Kim, H. Lee, M. Y. Zhuravlev, C. B. Eom, E. Y. Tsymbal, A. Sinitskii, and A. Gruverman, Ferroelectric tunnel junctions with graphene electrodes, Nature Communications **5**, 5518 (2014).
[22] W. Park, J. H. Yang, C. G. Kang, Y. G. Lee, H. J. Hwang, C. Cho, S. K. Lim, S. C. Kang, W. K. Hong, S. K. Lee, S. Lee, and B. H. Lee, Characteristics of a pressure sensitive touch sensor using a piezoelectric PVDF-TrFE/MoS_2 stack, Nanotechnology **24**, 475501 (2013).
[23] A. Rajapitamahuni, J. Hoffman, C. H. Ahn, and X. Hong, Examining Graphene Field Effect Sensors for Ferroelectric Thin Film Studies, Nano Letters **13**, 4374 (2013).

[24] C. Ma, Y. Gong, R. Lu, E. Brown, B. Ma, J. Li, and J. Wu, Detangling Extrinsic and Intrinsic Hysteresis for Detecting Dynamic Switch of Electric Dipoles using Graphene Field-Effect Transistors on Ferroelectric Gates, Nanoscale **7**, 18489 (2015).
[25] A. Lipatov, P. Sharma, A. Gruverman, and A. Sinitskii, Optoelectrical Molybdenum Disulfide (MoS_2)—Ferroelectric Memories, ACS Nano **9**, 8089 (2015).
[26] X. Wang, P. Wang, J. Wang, W. Hu, X. Zhou, N. Guo, H. Huang, S. Sun, H. Shen, T. Lin, M. Tang, L. Liao, A. Jiang, J. Sun, X. Meng, X. Chen, W. Lu, and J. Chu, Ultrasensitive and Broadband MoS_2 Photodetector Driven by Ferroelectrics, Advanced Materials **27**, 6575 (2015).
[27] M. D. Goldflam, G.-X. Ni, K. W. Post, Z. Fei, Y. Yeo, J. Y. Tan, A. S. Rodin, B. C. Chapler, B. Özyilmaz, A. H. Castro Neto, M. M. Fogler, and D. N. Basov, Tuning and Persistent Switching of Graphene Plasmons on a Ferroelectric Substrate, Nano Letters **15**, 4859 (2015).
[28] C. H. Li, K. M. McCreary, and B. T. Jonker, Spatial Control of Photoluminescence at Room Temperature by Ferroelectric Domains in Monolayer WS_2/PZT Hybrid Structures, Acs Omega **1**, 1075 (2016).
[29] S. Ducharme, S. P. Palto, V. M. Freidkin, and L. M. Blinov, in *Handbook of Thin Film Materials*, edited by H. S. Nalwa (Academic, San Diego, 2002).
[30] M. J. Bai, A. V. Sorokin, D. W. Thompson, M. Poulsen, S. Ducharme, C. M. Herzinger, S. Palto, V. M. Fridkin, S. G. Yudin, V. E. Savchenko, and L. K. Gribova, Determination of the optical dispersion in ferroelectric vinylidene fluoride (70%)/trifluoroethylene (30%) copolymer Langmuir-Blodgett films, Journal of Applied Physics **95**, 3372 (2004).
[31] See Supplemental Material at [URL will be inserted by publisher] for the detials on sample preparation, electrical characterization, and data modeling, which include Refs. [32-36].
[32] C. Lee, H. Yan, L. E. Brus, T. F. Heinz, J. Hone, and S. Ryu, Anomalous Lattice Vibrations of Single- and Few-Layer MoS2, Acs Nano **4**, 2695 (2010).
[33] A. Splendiani, L. Sun, Y. B. Zhang, T. S. Li, J. Kim, C. Y. Chim, G. Galli, and F. Wang, Emerging Photoluminescence in Monolayer MoS2, Nano Lett **10**, 1271 (2010).
[34] B. Chakraborty, A. Bera, D. V. S. Muthu, S. Bhowmick, U. V. Waghmare, and A. K. Sood, Symmetry-dependent phonon renormalization in monolayer MoS_2 transistor, Phys Rev B **85** (2012).
[35] T. Jin, J. Kang, E. S. Kim, S. Lee, and C. Lee, Suspended single-layer MoS2 devices, J Appl Phys **114** (2013).
[36] K. Kaasbjerg, K. S. Thygesen, and K. W. Jacobsen, Phonon-limited mobility in *n*-type single-layer MoS_2 from first principles, Physical Review B **85**, 115317 (2012).
[37] Z. Xiao, S. Poddar, S. Ducharme, and X. Hong, Domain wall roughness and creep in nanoscale crystalline ferroelectric polymers, Applied Physics Letters **103**, 112903 (2013).
[38] Z. Xiao, J. Hamblin, S. Poddar, S. Ducharme, P. Paruch, and X. Hong, Effect of thermal annealing on ferroelectric domain structures in poly(vinylidene-fluoride-trifluorethylene) Langmuir-Blodgett thin films, Journal of Applied Physics **116**, 066819 (2014).
[39] C. Jang, S. Adam, J. H. Chen, D. Williams, S. Das Sarma, and M. S. Fuhrer, Tuning the effective fine structure constant in graphene: Opposing effects of dielectric screening on short- and long-range potential scattering, Physical Review Letters **101**, 146805 (2008).
[40] K. Zou, X. Hong, D. Keefer, and J. Zhu, Deposition of High-Quality HfO_2 on Graphene and the Effect of Remote Oxide Phonon Scattering, Physical Review Letters **105**, 126601 (2010).

[41] N. Ma, and D. Jena, Charge Scattering and Mobility in Atomically Thin Semiconductors, Physical Review X **4**, 011043 (2014).
[42] M. S. Fuhrer, and J. Hone, Measurement of mobility in dual-gated MoS_2 transistors, Nature Nanotechnology **8**, 146 (2013).
[43] K. S. Novoselov, D. Jiang, F. Schedin, T. J. Booth, V. V. Khotkevich, S. V. Morozov, and A. K. Geim, Two-dimensional atomic crystals, Proceedings of the National Academy of Sciences of the United States of America **102**, 10451 (2005).
[44] B. Radisavljevic, and A. Kis, Mobility engineering and a metal–insulator transition in monolayer MoS_2, Nature Materials **12**, 815 (2013).
[45] K. Tashiro, Y. Itoh, M. Kobayashi, and H. Tadokoro, Polarized Raman-Spectra and LO-TO Splitting of Poly (Vinylidene Fluoride) Crystal Form-I, Macromolecules **18**, 2600 (1985).
[46] M. V. Fischetti, D. A. Neumayer, and E. A. Cartier, Effective electron mobility in Si inversion layers in metal-oxide-semiconductor systems with a high-kappa insulator: The role of remote phonon scattering, Journal of Applied Physics **90**, 4587 (2001).
[47] J. Kunc, Y. K. Hu, J. Palmer, Z. L. Guo, J. Hankinson, S. H. Gamal, C. Berger, and W. A. de Heer, Planar Edge Schottky Barrier-Tunneling Transistors Using Epitaxial Graphene/SiC Junctions, Nano Letters **14**, 5170 (2014).

Captions

FIG. 1. (a) Device schematic. (b) Room-temperature transfer characteristics for sample D2 in the initial no poling state, and after the writing P(VDF-TrFE) with +10 V (1st poling), -10 V (2nd poling), and +10 V (3rd poling) tip bias. The arrows mark the corresponding V_ts. (c) The AFM topography image of the sample and the PFM phase images after (d) the 1st and (e) 2nd poling. The scale bars are 1 μm. The dotted lines outline the MoS_2 flake and the Au electrodes.

FIG. 2. (a) Calculated n_{total} (solid symbols) and n_{free} (open symbols) as a function of V_{bg} for sample D3 at $V_{bg} > V_t$ for both polarization states, and (b) the corresponding m_{band} as function of n_{free}.

FIG. 3. (a) Room-temperature I_{DS}-V_{DS} of sample D4 at V_{bg} = -10 V for the mono-domain states, and (b) the half P_{up}-half P_{down} state (open symbols) with a fit to Eq. (3) (solid line). Inset: PFM phase image of the domain structure. Scale bar: 1 mm. (c) Normalized I_{DS} vs. V_{DS} and V_{bg} for the half P_{up}-half P_{down} state. Superimposed on the plot are the transfer curves at V_{DS} = 100 mV for the uniform P_{up} and P_{down} states (right axis). The vertical arrows mark the V_ts. The dashed lines mark the boundaries separating regions I, II, and III.

FIG. 4. (a) I_{DS}-V_{DS} (open symbols) at V_{bg} = -10 V with a fit to Eq. (1) (solid line). Inset: Schematic band diagram for MoS_2 in the P_{up} and P_{down} states. (b) I_{DS}-V_{DS} (open symbols) at V_{bg} = -4 V with a fit to Eq. (2) (solid line). The dashed and dotted lines correspond to the first and second terms in Eq. (4), respectively. (c) I_{DS}-V_{DS} at V_{bg} = -10 V taken in the as-prepared state of P(VDF-TrFE) (black symbols) and after domain patterning and thermal depolarization (red line). (d) Φ_B^{eff} as a function of normalized V_{bg} for samples D3-D6.

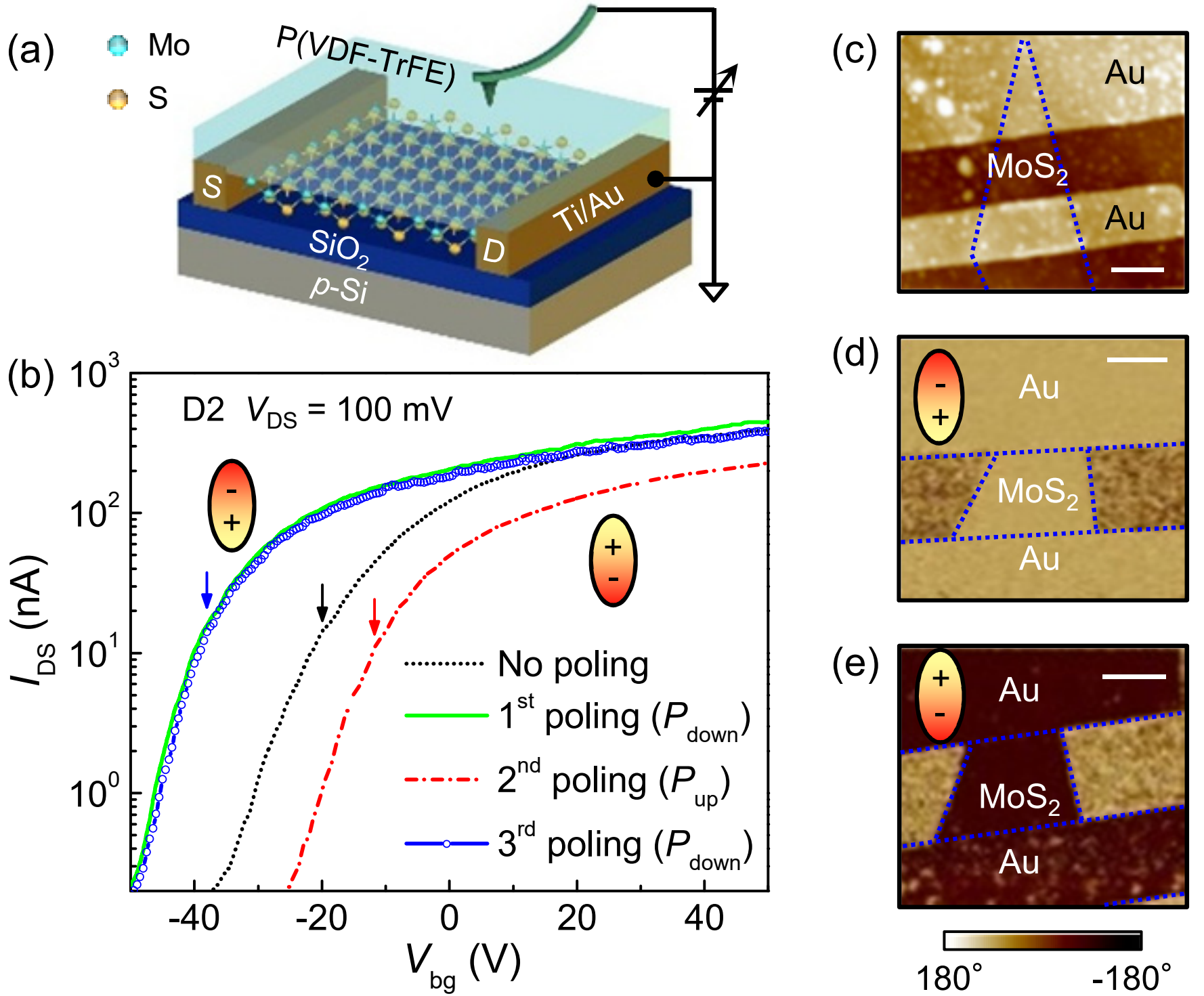
(a)
Mo
S
P(VDF-TrFE)
S
D
Ti/Au
SiO2
p-Si
(b)
D2 VDS = 100 mV
IDS (nA)
Vbg (V)
No poling
1st poling (Pdown)
2nd poling (Pup)
3rd poling (Pdown)
(c)
Au
MoS2
Au
(d)
Au
MoS2
Au
(e)
Au
MoS2
Au
180°
-180°

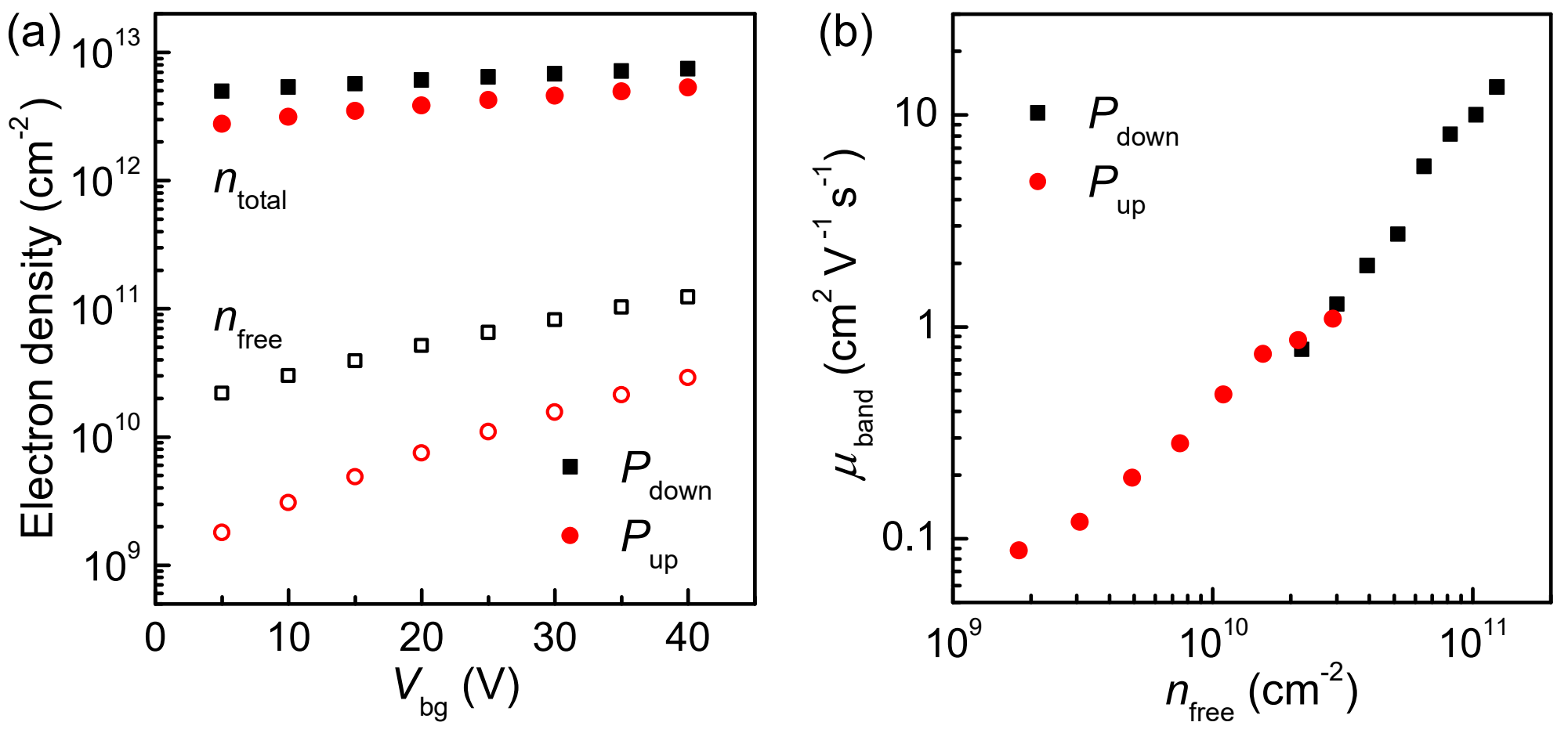
(a)
Electron density (cm^{-2})
10^{13}
10^{12}
10^{11}
10^{10}
10^{9}
n_{total}
n_{free}
P_{down}
P_{up}
0
10
20
30
40
V_{bg} (V)
(b)
μ_{band} (cm^2 V^{-1} s^{-1})
10
1
0.1
P_{down}
P_{up}
10^{9}
10^{10}
10^{11}
n_{free} (cm^{-2})

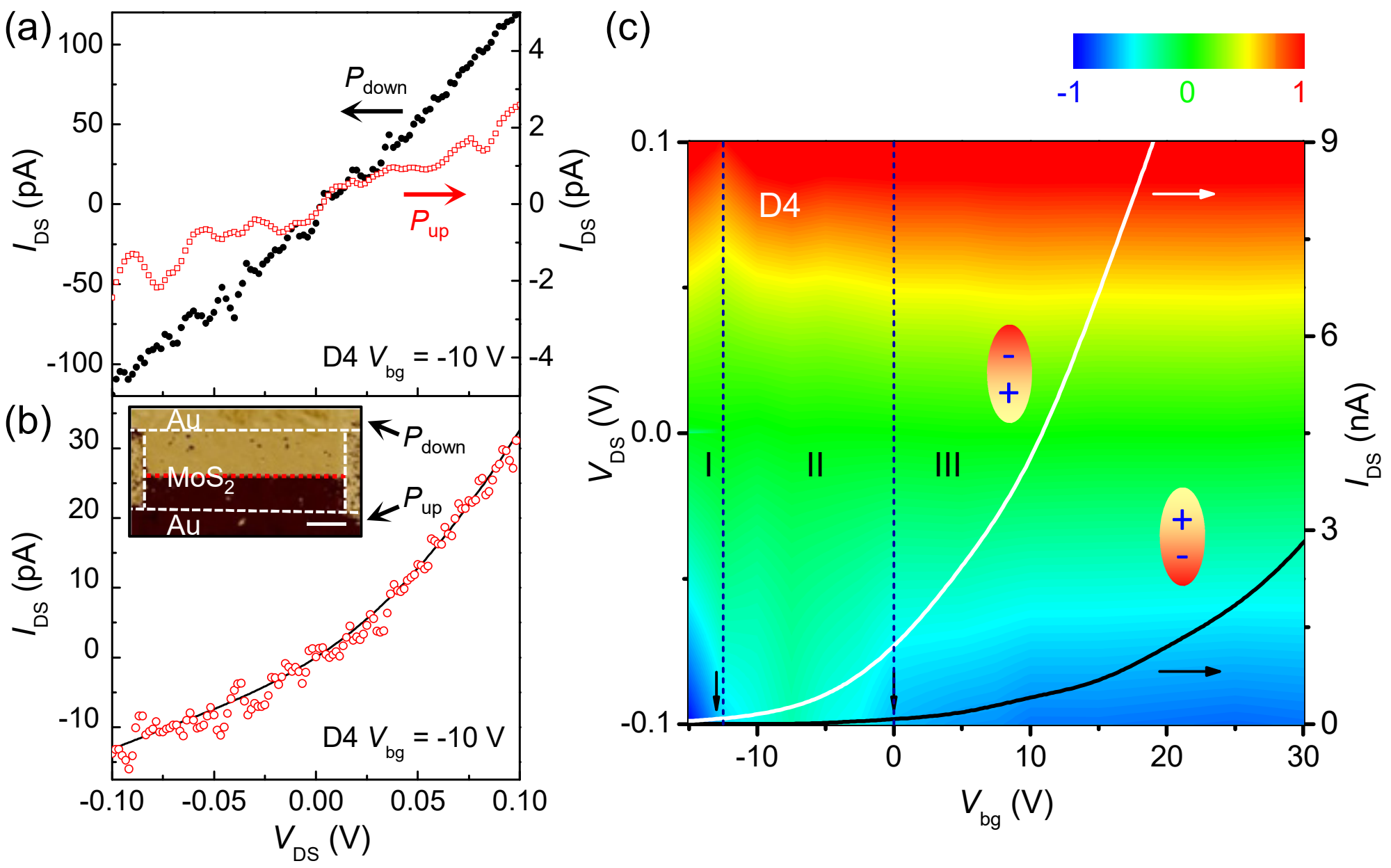
(a)
100
50
0
-50
-100
I_{DS} (pA)
P_{down}
P_{up}
D4 V_{bg} = -10 V
4
2
0
-2
-4
I_{DS} (pA)
(b)
Au
MoS_2
Au
P_{down}
P_{up}
30
20
10
0
-10
I_{DS} (pA)
D4 V_{bg} = -10 V
-0.10
-0.05
0.00
0.05
0.10
V_{DS} (V)
(c)
-1
0
1
0.1
0.0
-0.1
V_{DS} (V)
D4
I
II
III
-
+
+
-
9
6
3
0
I_{DS} (nA)
-10
0
10
20
30
V_{bg} (V)

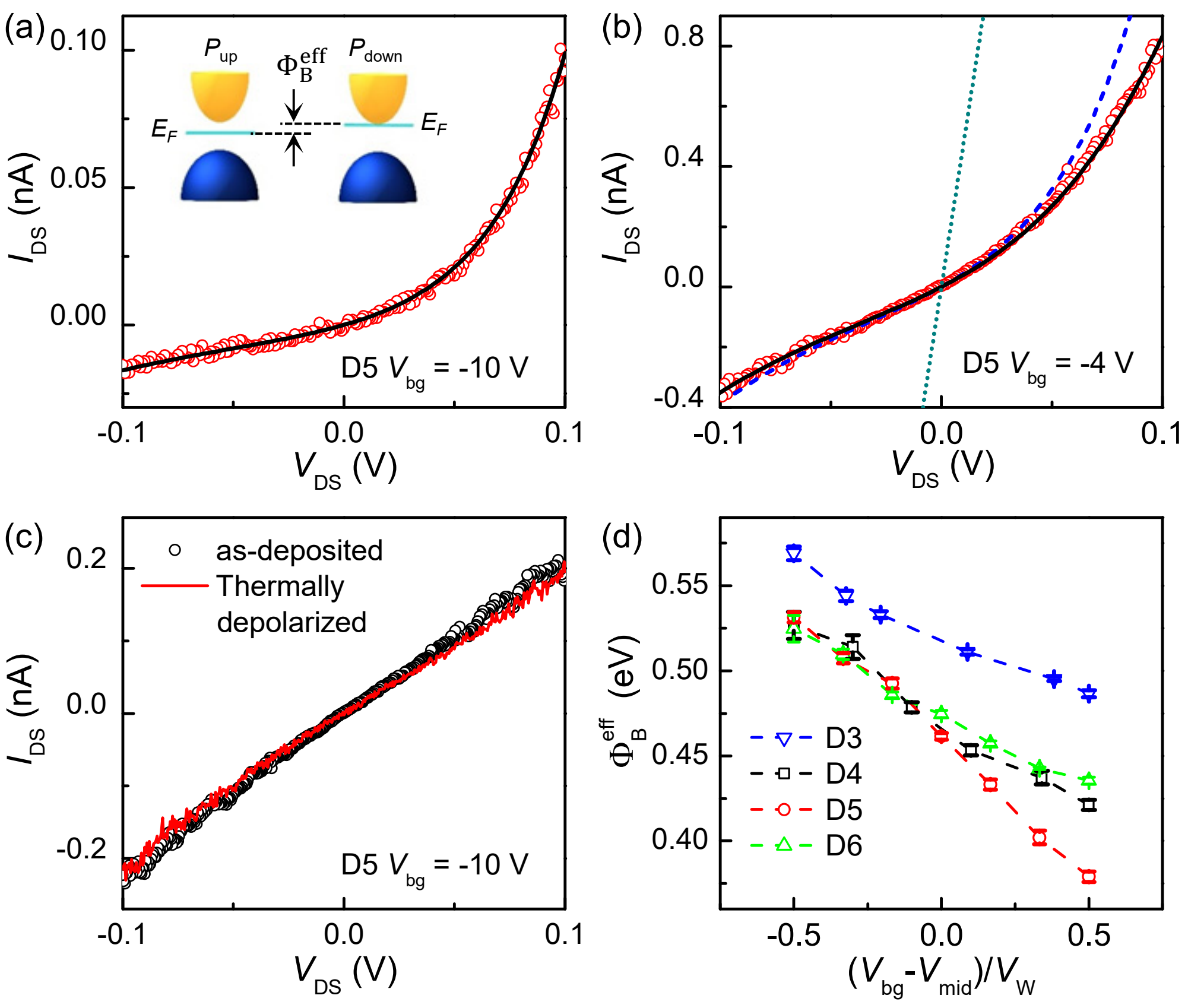
(a)
0.10
0.05
0.00
I_{DS} (nA)
P_{up}
Φ_B^{eff}
P_{down}
E_F
E_F
D5 V_{bg} = -10 V
-0.1
0.0
0.1
V_{DS} (V)
(b)
0.8
0.4
0.0
-0.4
I_{DS} (nA)
D5 V_{bg} = -4 V
-0.1
0.0
0.1
V_{DS} (V)
(c)
0.2
0.0
-0.2
I_{DS} (nA)
as-deposited
Thermally depolarized
D5 V_{bg} = -10 V
-0.1
0.0
0.1
V_{DS} (V)
(d)
0.55
0.50
0.45
0.40
Φ_B^{eff} (eV)
D3
D4
D5
D6
-0.5
0.0
0.5
$(V_{bg}-V_{mid})/V_W$